A unified framework for forward and inverse modeling of ice sheet flow using physics-informed neural networks

Gong Cheng[1], **Mathieu Morlighem**[1], **and Sade Francis**[1]

[1]Department of Earth Sciences, Dartmouth College, Hanover, NH 03755, USA

Key Points:

- We present a unified framework for solving forward and inverse problems in ice sheet modeling using physics-informed neural networks
- We are able to infer parameters that traditional numerical methods cannot invert for, such as ice thickness
- We show the capability of the framework: simultaneous inversion of basal friction while interpolating sparse ice thickness observations

Corresponding author: Gong Cheng, gong.cheng@dartmouth.edu

Abstract

Predicting the future contribution of the ice sheets to sea level rise over the next decades presents several challenges due to a poor understanding of critical boundary conditions, such as basal sliding. Traditional numerical models often rely on data assimilation methods to infer spatially variable friction coefficients by solving an inverse problem, given an empirical friction law. However, these approaches are not versatile, as they sometimes demand extensive code development efforts when integrating new physics into the model. Furthermore, this approach makes it difficult to handle sparse data effectively. To tackle these challenges, we propose a novel approach utilizing Physics-Informed Neural Networks (PINNs) to seamlessly integrate observational data and governing equations of ice flow into a unified loss function, facilitating the solution of both forward and inverse problems within the same framework. We illustrate the versatility of this approach by applying the framework to two-dimensional problems on the Helheim Glacier in southeast Greenland. By systematically concealing one variable (e.g. ice speed, ice thickness, etc.), we demonstrate the ability of PINNs to accurately reconstruct hidden information. Furthermore, we extend this application to address a challenging mixed inversion problem. We show how PINNs are capable of inferring the basal friction coefficient while simultaneously filling gaps in the sparsely observed ice thickness. This unified framework offers a promising avenue to enhance the predictive capabilities of ice sheet models, reducing uncertainties, and advancing our understanding of poorly constrained physical processes.

Plain Language Summary

Our ability to predict the future contribution of the ice sheets to future sea-level rise is limited due to the lack of observations, especially at the base of the ice sheets. Traditional computer models infer basal sliding from observations at the surface based on ice flow physics, a process that becomes complex and inflexible when incorporating new information or a more sophisticated description of ice flow. Our solution involves Physics-Informed Neural Networks that seamlessly integrate data and physical laws in a unified framework. We demonstrate the versatility of PINNs on Helheim Glacier in Southeast Greenland, showcasing their ability to handle missing or incomplete data. Additionally, we extend PINNs to address a challenging problem, which consists of inferring basal sliding while filling gaps in sparsely observed ice thickness at the same time. This unified approach holds promise for improving ice sheet predictions and advancing our understanding of complex ice dynamics.

1 Introduction

The Greenland and Antarctic ice sheets are collectively responsible for more than half of the observed global sea-level rise in recent decades (Frederikse et al., 2020). This mass loss is primarily driven by the dynamic behavior of marine-terminating glaciers, which discharge icebergs into the ocean (Mouginot et al., 2019; Rignot et al., 2019). Current projections of sea level rise rely on transient simulations (Nowicki et al., 2016; Eyring et al., 2016) that capture the response of these outlet glaciers to climate forcings. These numerical models solve forward problems to compute the evolution of ice velocity and geometry (Durand et al., 2009; Mangeney & Califano, 1998; Bueler & Brown, 2009; Colinge & Blatter, 1998), which, in turn, affect the discharge of ice into the ocean.

Among all the physical processes influencing current and future ice discharge, basal friction is a major control on the dynamics of these outlet glaciers. Basal friction characterizes a relationship between the ice basal velocity and the stress exerted by the underlying bed (Budd et al., 1979; Weertman, 1957; Gagliardini et al., 2007). This relationship has a significant influence on how the ice sheets respond to external forcings, particularly in the context of climate change (Yu et al., 2018; Brondex et al., 2019; Barnes

et al., 2021). Therefore, improving our understanding of basal conditions and accurately representing them in ice sheet numerical models is critical (Brondex et al., 2017; Åkesson et al., 2021).

Empirical friction laws typically incorporate a friction "coefficient", which is spatially and sometimes temporally variable, encapsulating less-understood physical processes. This friction coefficient cannot be directly measured and is generally inferred from surface observations using data assimilation methods (Tarantola, 2005; D. MacAyeal, 2002; Petra et al., 2012; Morlighem et al., 2013). These methods involve solving inverse problems aimed at minimizing an objective or cost function, which is constructed based on the misfit between observed and modeled variables, such as surface velocity or surface elevation (Goldberg & Sergienko, 2011; Morlighem & Goldberg, 2023). These observational data are often associated with noise, and the uncertainties, as well as model error, propagate through the inverse model and end up lumped into the friction coefficient (Karniadakis et al., 2021; Cheng & Lotstedt, 2020), which contributes significantly to the overall uncertainty in ice sheet modeling. Furthermore, solving inverse problems often requires specially designed numerical methods, demanding different formulations and sometimes complex computer codes (Griewank et al., 1996; Vogel, 2002). These challenges underscore the pressing need for novel approaches to potentially alleviate these issues and enhance our ability to model and understand the dynamics of ice sheets.

Recent advances in Machine Learning techniques together with the wealth of new remote sensing data offer opportunities to develop new approaches to better constrain numerical models with data. Physics-Informed Neural Networks, for example, have been specifically designed to tackle complex problems associated with intricate mathematical operations (Raissi et al., 2019; Karniadakis et al., 2021; Lu et al., 2021). PINNs seamlessly integrate observational data with underlying physical laws and have been used in a wide range of applications (e.g., Lu et al., 2021; Karniadakis et al., 2021; Riel et al., 2021). The PINN loss function represents a weighted sum of data misfits and the residuals of the governing equations, typically in the form of partial differential equations (PDEs). This contrasts with standard deep neural networks, which solely learn from available data. By enforcing physical laws as soft constraints, PINNs make it possible to infer quantities without direct observations.

Here, we explore the use of PINNs in ice sheet modeling by solving two-dimensional forward and inverse problems on a real Greenland glacier. By training PINNs with a carefully designed loss function, while knowing all variables except one, we try to recover the unknown. Depending on the choice of training data, we use this framework as a forward solver to get the ice velocity, or as an inverse solver to infer the basal friction coefficient. To evaluate whether PINNs can effectively and accurately reconstruct the hidden information, we compare its solution with the true solution obtained from a conventional numerical model. Furthermore, we try to infer other parameters within the governing equations using this framework, even those challenging to invert using traditional numerical methods. In a second set of experiments, we extend the application of PINNs to address a challenging mixed-inversion problem: we test the ability of the framework to infer the basal friction coefficient while simultaneously filling in gaps in sparsely observed ice thickness. This mixed inversion problem represents a class of scenarios that has not yet been explored by conventional numerical methods due to its intrinsic complexity.

2 Method

2.1 The physics-informed neural networks

Following Raissi et al. (2019), we implement a PINN to assimilate both the physical model detailed in section 2.2 and the data presented in section 2.3. The architecture of the PINN is schematically illustrated in Figure 1. In this configuration, fully con-

nected parallel neural networks are employed, with the inputs designated as the coordinates x and y in the two-dimensional plane (or x in the one-dimensional cases). The PINN generates predictions for five different outputs. Specifically, three parallel neural networks, each comprising 6 layers with 20 neurons per layer, are utilized to generate predictions for ice velocity, ice geometry, and friction coefficient, respectively. We employ the hyperbolic tangent activation function for all neurons in the PINN. To ensure the reliability of the network predictions, we normalize the input variables to the range $[-1, 1]$ across the computational domain before feeding them into the network. Additionally, the network outputs are denormalized from the range $[-1, 1]$ to their actual values as used in the governing PDEs.

The total loss function, $\mathcal{L}$, comprises two parts. The first component captures the total data misfit at locations where observational data are available. The second component captures the residual of the governing PDEs at a set of randomly selected collocation points. The training process involves optimizing the loss function with respect to the coefficients of the neural networks, which strikes a balance between fitting the available data and satisfying the physical equations that govern the ice sheet flow.

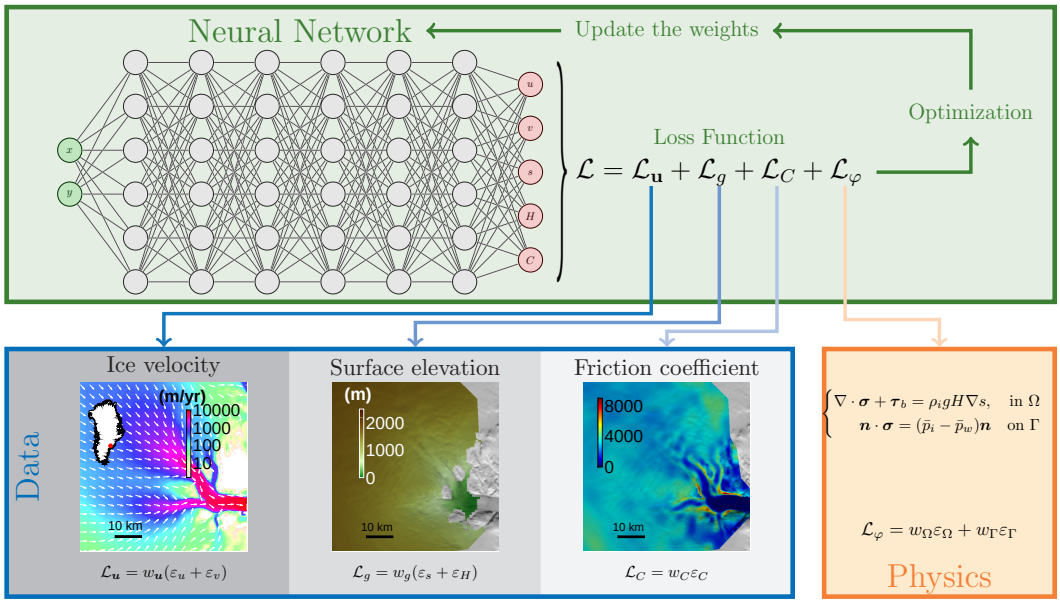

Figure 1. Illustration of the Physics-Informed Neural Network. Note that the neural network architecture depicted here is for illustrative purposes only, and does not represent the actual configuration used in this study described in the text.

2.2 Physical model – Shelfy Stream Approximation

Consider a two-dimensional domain $\boldsymbol{x} = (x, y) \in \Omega$, where the ice velocity is denoted as $\boldsymbol{u} = (u, v)^T$. The governing ice dynamics are described by the Shelfy Stream Approximation (MacAyeal, 1989, SSA), expressed as a system of PDEs:

$$\nabla \cdot \boldsymbol{\sigma} + \boldsymbol{\tau}_b = \rho_i g H \nabla s \tag{1}$$

where $\boldsymbol{\tau}_b = (\tau_{bx}, \tau_{by})^T$ represents the basal shear stress, ρ_i is the ice density, g is the gravitational acceleration. $\boldsymbol{\sigma}$ is the stress tensor of the SSA model defined as

$$\boldsymbol{\sigma} = \mu H \begin{bmatrix} 4\frac{\partial u}{\partial x} + 2\frac{\partial v}{\partial y} & \frac{\partial u}{\partial y} + \frac{\partial v}{\partial x} \\ \frac{\partial u}{\partial y} + \frac{\partial v}{\partial x} & 2\frac{\partial u}{\partial x} + 4\frac{\partial v}{\partial y} \end{bmatrix}. \tag{2}$$

The ice viscosity, μ, is determined by Glen's flow-law (Glen, 1958), which in two dimensions reads:

$$\mu = \frac{B}{2}\left(\left(\frac{\partial u}{\partial x}\right)^2 + \left(\frac{\partial v}{\partial y}\right)^2 + \frac{1}{4}\left(\frac{\partial u}{\partial y} + \frac{\partial v}{\partial x}\right)^2 + \frac{\partial u}{\partial x}\frac{\partial v}{\partial y}\right)^{\frac{1-n}{2n}}, \tag{3}$$

where $n = 3$ is the flow-law exponent, and B is the pre-factor dependent on ice temperature (Cuffey & Paterson, 2010), among other factors.

We assume here that the basal shear stress $\boldsymbol{\tau}_b$ is related to the ice velocity $\boldsymbol{u}$ by Weertman's friction law (Weertman, 1957)

$$\boldsymbol{\tau}_b = -C^2 |\boldsymbol{u}|^{m-1} \boldsymbol{u}, \tag{4}$$

where C is a spatially varying friction coefficient and $m = 1/3$. While various empirical friction laws exist (e.g., Budd et al., 1979; Weertman, 1957; Gagliardini et al., 2007), for simplicity, we focus on Weertman's law in this work. Nevertheless, the methodology presented can be generalized to accommodate other friction laws.

Many of the Greenlandic glaciers are marine-terminating glaciers, which have calving fronts at the ice-ocean interface. The boundary conditions on the calving front Γ are defined as

$$\mathbf{n} \cdot \boldsymbol{\sigma} = \frac{1}{2} g \left(\rho_i H^2 - \rho_w b^2\right) \mathbf{n} \tag{5}$$

where $\mathbf{n} = (n_x, n_y)^T$ is the outward normal unit vector on Γ, ρ_w is the density of sea water, and $b = s - H$ is the bed elevation. For the remaining outer boundaries of the domain, we apply Dirichlet boundary conditions.

2.3 Data

We rely on a diverse set of observations from both direct measurements and reanalysis models. These datasets include ice velocity, surface elevation, ice front positions, ice thickness, and inferred basal friction coefficients. In this work, we use the data from Helheim Glacier in Southeast Greenland, as shown in Figure 2.

The ice surface velocity mosaic is from NASA's MEaSUREs products (Joughin et al., 2018). We denote the velocity observations at $N_{\boldsymbol{u}}$ distinct locations $\{\boldsymbol{x}_j^{\boldsymbol{u}}\}_{j=1}^{N_{\boldsymbol{u}}}$ as $\hat{\boldsymbol{u}}_j = (\hat{u}_j, \hat{v}_j)^T$. Surface elevation data $\hat{s}_j$ at the location $\{\boldsymbol{x}_j^s\}_{j=1}^{N_s}$ are from the Greenland Ice Mapping Project (Howat et al., 2014), while ice thickness $\hat{H}_j$ at $\{\boldsymbol{x}_j^H\}_{j=1}^{N_H}$ is from BedMachine Greenland v6.1 (Morlighem et al., 2017). The ice front position is derived using the ice mask from Howat et al. (2014).

To train and validate the PINNs, we require the friction coefficient $\hat{C}_j$ at some location $\{\boldsymbol{x}_j^C\}_{j=1}^{N_C}$. Since there is no direct observation of the friction coefficient, we perform an inversion using the Ice-sheet and Sea-level System Model (ISSM, Larour et al., 2012), using the aforementioned datasets to infer the friction coefficient following the method described in Morlighem et al. (2013).

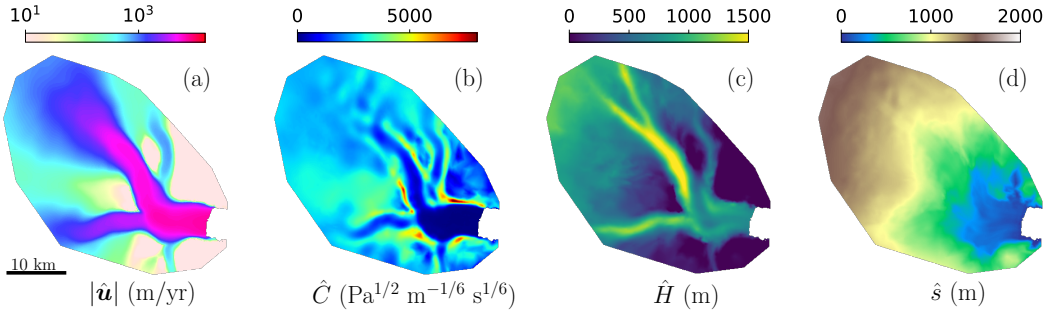

Figure 2. Reference data from Helheim Glacier. (a) velocity magnitude (b) basal friction coefficient (c) ice thickness (d) surface elevation.

2.4 The loss function

We formulate a loss function $\mathcal{L}(\theta)$ to optimize the coefficients θ of the neural networks. This loss function takes the form

$$\mathcal{L} = \mathcal{L}_{\boldsymbol{u}} + \mathcal{L}_g + \mathcal{L}_C + \mathcal{L}_\varphi \tag{6}$$

where each term represents the contributions to the loss function associated with subscripts $\boldsymbol{u}$ (velocity), g (ice geometry), C (friction coefficients), and φ (PDE residuals). Specifically, our loss function comprises a weighted sum of data misfits and residuals from the governing PDEs. We further denote these misfits and residuals by ε, and the weights by w, with the same subscripts as the ones described above.

The data misfits are calculated by the mean-square errors (MSE) of the PINN's predictions at locations where the corresponding observational data is available, and they contribute to the loss function as

$$\mathcal{L}_{\boldsymbol{u}} = w_{\boldsymbol{u}}(\varepsilon_u + \varepsilon_v) = \frac{w_{\boldsymbol{u}}}{N_{\boldsymbol{u}}} \sum_{j=1}^{N_u} \left(\left(u(\boldsymbol{x}_j^u) - \hat{u}_j\right)^2 + \left(v(\boldsymbol{x}_j^u) - \hat{v}_j\right)^2 \right), \tag{7}$$

$$\mathcal{L}_g = w_g(\varepsilon_s + \varepsilon_H) = \frac{w_g}{N_s} \sum_{j=1}^{N_s} \left(s(\boldsymbol{x}_j^s) - \hat{s}_j\right)^2 + \frac{w_g}{N_H} \sum_{j=1}^{N_H} \left(H(\boldsymbol{x}_j^H) - \hat{H}_j\right)^2, \tag{8}$$

$$\mathcal{L}_C = w_C \varepsilon_C = \frac{w_C}{N_C} \sum_{j=1}^{N_C} \left(C(\boldsymbol{x}_j^C) - \hat{C}_j\right)^2, \tag{9}$$

where $u(\boldsymbol{x}), v(\boldsymbol{x}), s(\boldsymbol{x}), H(\boldsymbol{x})$, and $C(\boldsymbol{x})$ are the output of the PINN as shown in Figure 1. The weights, $w_{\boldsymbol{u}}$, w_g, and w_C, are scaled according to the typical values of the ice velocity, ice thickness, and friction coefficient in the International System of Units (SI), to balance their contributions to the total loss function. For Helheim Glacier, the typical values of these variables and the corresponding weights are shown in Table 1.

The PDEs in (1) are evaluated using the output of the PINN at a distinct set of collocation points $\{\boldsymbol{x}_j^\Omega\}_{j=1}^{N_\Omega}$, which are different from the observational datasets in section 2.3. The residual of the PDEs is expressed as the mean-square errors among these collocation points together with the boundary conditions. Specifically, for the Helheim Glacier, we include the calving front boundary condition along the points at $\{\boldsymbol{x}_j^\Gamma\}_{j=1}^{N_\Gamma}$ in evaluating the residual of the PDEs as

$$\mathcal{L}_\varphi = w_\Omega \varepsilon_\Omega + w_\Gamma \varepsilon_\Gamma = \frac{w_\Omega}{N_\Omega} \sum_{i=1}^{N_\Omega} \|\nabla \cdot \boldsymbol{\sigma} + \boldsymbol{\tau}_b - \rho_i g H \nabla s\|^2 + \frac{w_\Gamma}{N_\Gamma} \sum_{i=1}^{N_\Gamma} \left\| \mathbf{n} \cdot \boldsymbol{\sigma} - \frac{1}{2} g \left(\rho_i H^2 - \rho_w b^2\right) \mathbf{n} \right\|^2, \tag{10}$$

Table 1. Typical values of variables in Helheim Glacier

variable	typical value	weights	value
$\lvert\boldsymbol{u}\rvert$	10^4 m yr^{-1}	$w_{\boldsymbol{u}}$	$10^{-8} \times (31536000^2)$ m^{-2} s^2
s, H	10^3 m	w_g	10^{-6} m^{-2}
C	10^4 Pa$^{1/2}$m$^{-1/6}$s$^{1/6}$	w_C	10^{-8} Pa^{-1} m$^{1/3}$ s$^{-1/3}$
$\boldsymbol{\tau}_b$	10^5 Pa	w_Ω	10^{-10} Pa^{-2}
$\rho_i g H^2$	10^9 Pa m	w_Γ	10^{-18} Pa^{-2}m^{-2}

where the weights w_Ω and w_Γ are chosen by scaling the basal shear stress and boundary force as in Table 1.

Effectively constructing a robust loss function for the PINN poses a significant challenge due to the diverse nature of its components, each representing distinct physical quantities with inherently different orders of magnitudes. Importantly, these components serve as soft constraints within the loss function, collectively influencing the learning process of the neural network (Iwasaki & Lai, 2023; Lu et al., 2021). The success of PINNs in ice sheet modeling critically relies on the careful selection of weights assigned to each component in the loss function. To optimize the predictive capabilities of the PINN before applying it to real problems at Helheim Glacier, we perform an extensive grid search to find the best weights outlined in Table 1. We fix $w_{\boldsymbol{u}}$ and vary the other four weights by several orders of magnitude around the typical values. This search aims to validate that the values in Table 1 are indeed optimal for the diverse components in the loss function. We systematically vary w_g and w_C by ± 2 orders of magnitude, while adjusting w_Ω by ± 5 orders of magnitude. For w_Γ, the ratio w_Ω / w_Γ is fixed at 10^{-8}. To ensure robustness, each experiment is repeated at least 25 times using a Glorot normal initializer with distinct random seeds. To speed up the grid search procedure, we perform these validation experiments exclusively on an inverse problem along a flowline of Helheim Glacier, treating it as a one-dimensional problem with fewer data points. The main results are shown in section 3.1.

2.5 Numerical experiments

After validating the choice of the weights, we apply the PINN to the two-dimensional datasets obtained from Helheim Glacier, as detailed in section 2.3. Subsequently, we conduct three distinct sets of numerical experiments by intentionally concealing one component within the observational datasets.

In the first experiment, we test the ability of the PINN to solve the forward problem. This involves utilizing the friction coefficient, $\hat{C}$, and the ice geometry, $\hat{s}$ and $\hat{H}$, to solve for the ice velocity, $\boldsymbol{u}$. The second experiment tests the ability of the PINN to solve an inverse problem and infer basal friction based on observed velocities. Here, we train the network with ice velocity, $\hat{\boldsymbol{u}}$, and ice geometry, $\hat{s}$ and $\hat{H}$, and infer the basal friction coefficient, C. In the third experiment, we test the ability of the PINN to infer the ice thickness, H. This is accomplished using the ice velocity, $\hat{\boldsymbol{u}}$, surface elevation, $\hat{s}$, and the basal friction coefficient, $\hat{C}$, as training datasets.

For all three experiments, we use $4,000$ data points for the training sets, and $9,000$ collocation points for evaluating the PDE residual. The calving front is described by 121 data points with spacing of 200 m, and the Dirichlet boundary around the domain has 541 data points. All the experiments are trained with Adam optimization up to $1,000,000$ epochs on the NVIDIA Tesla V100 SXM2 32GB GPU. We use TensorFlow 2.4.1 imple-

Table 2. RMSE for all experiments

Experiments	$\lvert\boldsymbol{u}\rvert$ (m/yr)	C ($\mathrm{Pa}^{1/2}\ \mathrm{m}^{-1/6}\ \mathrm{s}^{1/6}$)	H (m)	s (m)
Forward problem	193.75	269.54	30.33	26.99
Inverse problem	56.01	589.61	18.96	14.11
Invert for H	70.64	114.55	69.47	12.99
Dual inversion	126.83	899.53	88.39	22.08

mentation of the Adam optimizer, with a learning rate at 0.001, $\beta_1 = 0.99$, $\beta_2 = 0.999$, and $\epsilon = 0.1$.

3 Results

3.1 Choice of weights

In total, we conducted over $15,000$ experiments, systematically exploring various combinations of weights. Perhaps unsurprisingly, balancing the different data misfits is relatively straightforward by scaling to the same magnitude within the SI unit system. However, the balance between the data misfit and PDE residual is particularly delicate in order to obtain satisfactory results.

In Figure 3, we vary w_Ω while keeping all other weights fixed, as specified in Table 1. Each point in the figure represents an experiment, and due to randomization in the training process, we repeated these experiments multiple times to derive an average behavior of the PINN. Figures 3 (a)-(c) exhibit distinct 'L-curve' patterns. As w_Ω decreases from 10^{-7} to 10^{-15} Pa^{-2}, the data misfit diminishes, reflecting the increased focus of the loss function on the data, while placing less emphasis on the PDE constraints. The minimum data misfit is achieved at $w_\Omega = 10^{-11}$ Pa^{-2}. However, errors, particularly the MSE of the velocity, start to diverge, which is indicative of overfitting. This trend becomes more pronounced for $w_\Omega < 10^{-11}$ Pa^{-2}. Figure 3 (d) further illustrates this by presenting the mean and standard deviation of test errors for each w_Ω. Test error is computed by comparing the PINN's prediction of C with the reference data $\hat{C}$. From this figure, we conclude that the optimal choice for w_Ω is 10^{-10} Pa^{-2}. This value corresponds to the square of 1/(100 kPa), a typical driving stress in ice sheet modeling, serving as the right-hand side of the PDE. This choice of weight aligns well with physical expectations.

3.2 Forward problem

Now that we know how to best choose the weights of the cost functions, we can perform our first set of experiments. We train the PINN with the dataset of friction coefficient, $\hat{C}$, ice thickness, $\hat{H}$, and surface elevation, $\hat{s}$, described in section 2.3. In this case, the PINN is treated as a solver for the forward problem, aiming to determine the ice velocity $\boldsymbol{u}$. Since we are not exposing the ice velocity to the PINN, the ice velocity is solely inferred by the PDE constraint in the loss function. The PINN's predictions and the corresponding misfits with respect to the reference data are shown in Figure 4. All predictions agree well with the reference data in Figure 2, particularly where training data is available, i.e., C, H, and s, as shown in Figure 4 (f-h). The root mean squared error (RMSE) of these misfits is presented in Table 2.

The PINN's prediction of the flow velocity closely matches the true solution over most of the area, capturing all branches of Helheim Glacier. Although there are some large misfits locally (e.g., ±700 m/yr) in the fast flow region, the RMSE of the misfit is

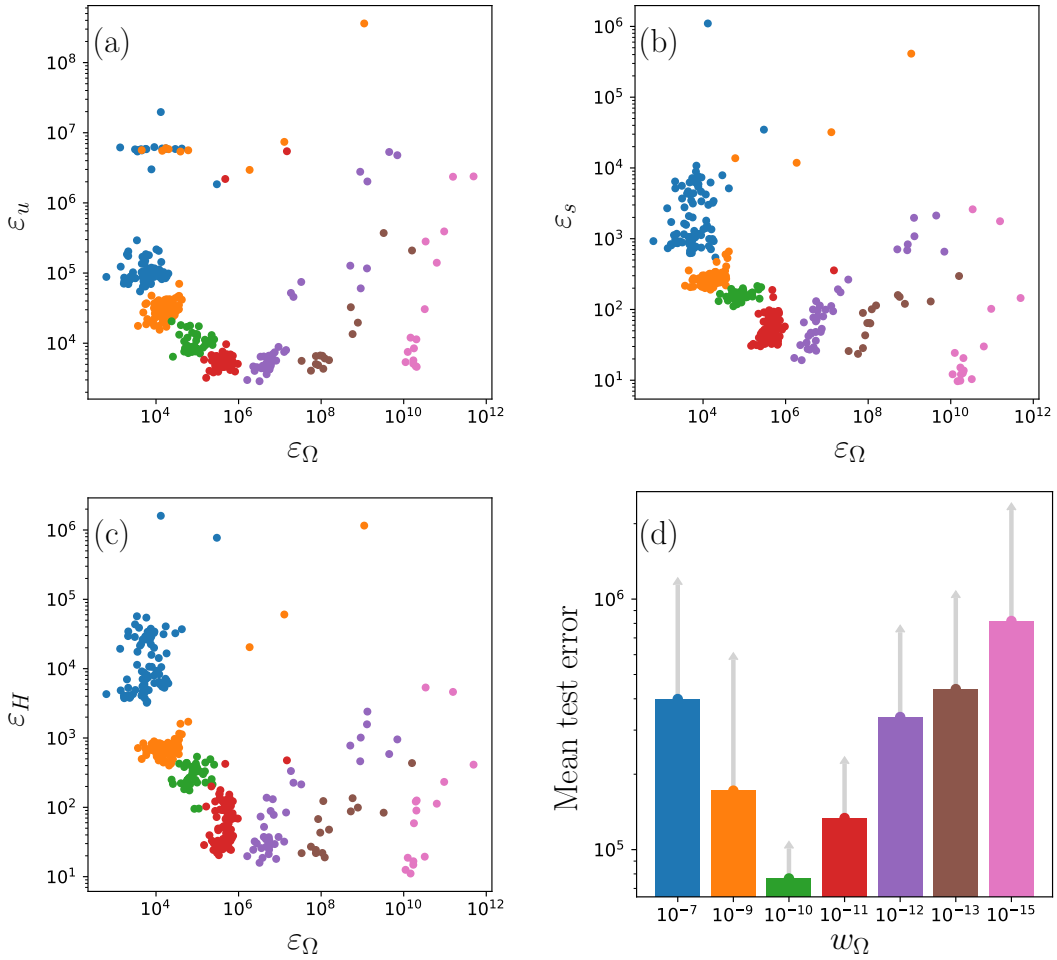

Figure 3. MSE of the (a) velocity, (b) surface elevation, and (c) ice thickness versus the PDE residual ε_Ω. (d) The mean test error of the PINNs predictions using different weights w_Ω.

193.75 m/yr. This represents approximately less than 10% of the average flow velocity over the entire domain (2,028.69 m/yr) and about 2.7% of the highest velocity (7,152.93 m/yr).

3.3 Inverse problem

We change the training dataset to use ice velocity $\hat{\boldsymbol{u}}$, ice thickness $\hat{H}$, and surface elevation $\hat{s}$. In this configuration, the PINN serves as an inverse solver to infer the basal friction coefficient C. Again, because we don't expose the PINN to the "true" friction coefficient from the ISSM model inversion, the PINN is inferring C solely based on the PDE constraint that is linking the friction coefficient to the other variables that the PINN is exposed to. The predictions and misfits are presented in Figure 5, and the RMSE of the misfit is provided in Table 2. Similar to the forward problem in section 3.2, the predictions of PINN align well with the "true" solution. Particularly for those learning from the reference data, the relative errors are all below 3% (the average ice thickness is 716.61 m, and the average surface elevation is 987.66 m).

The RMSE of the misfit in C is 589.61 $\text{Pa}^{1/2}$ $\text{m}^{-1/6}$ $\text{s}^{1/6}$. However, as shown in Figure 5(f), the pattern of large errors is located primarily in the slow-moving region (ve-

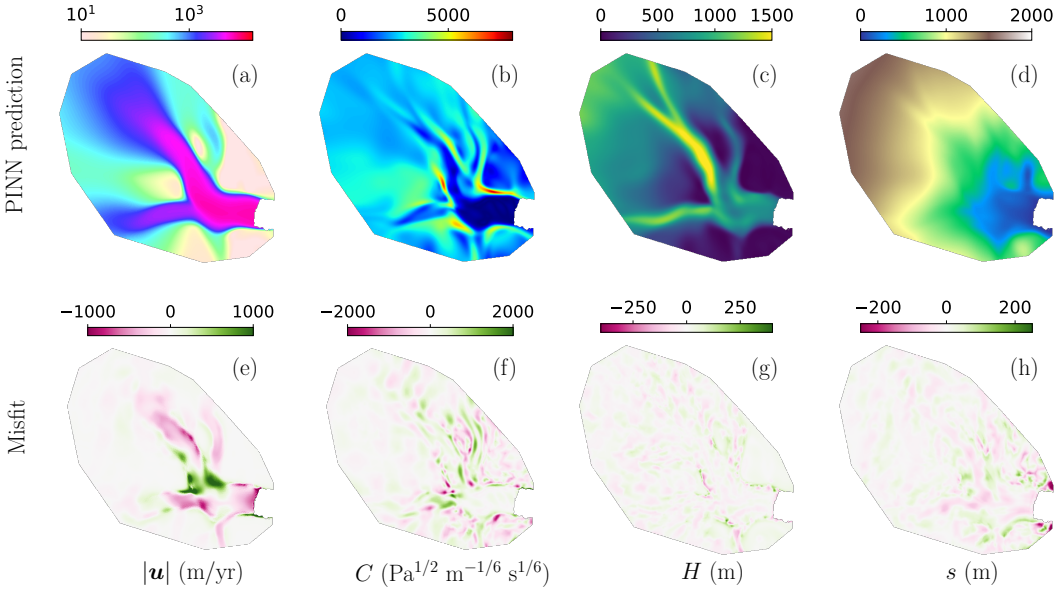

Figure 4. (a)-(d) Predictions of the PINN solving a forward problem without exposure to ice velocity during training. (e)-(h) Corresponding misfits between the predictions and the "true" velocity in Figure 2.

locity < 10 m/yr), where there is minimal ice coverage (ice thickness < 30 m). In contrast, the predicted friction coefficient is highly accurate in the fast-flow region, capturing all features, including branches and shear margins. The RMSE of misfit in C over the region with $|\boldsymbol{u}| > 10$ is 392.54 $\mathrm{Pa}^{1/2}$ $\mathrm{m}^{-1/6}$ $\mathrm{s}^{1/6}$.

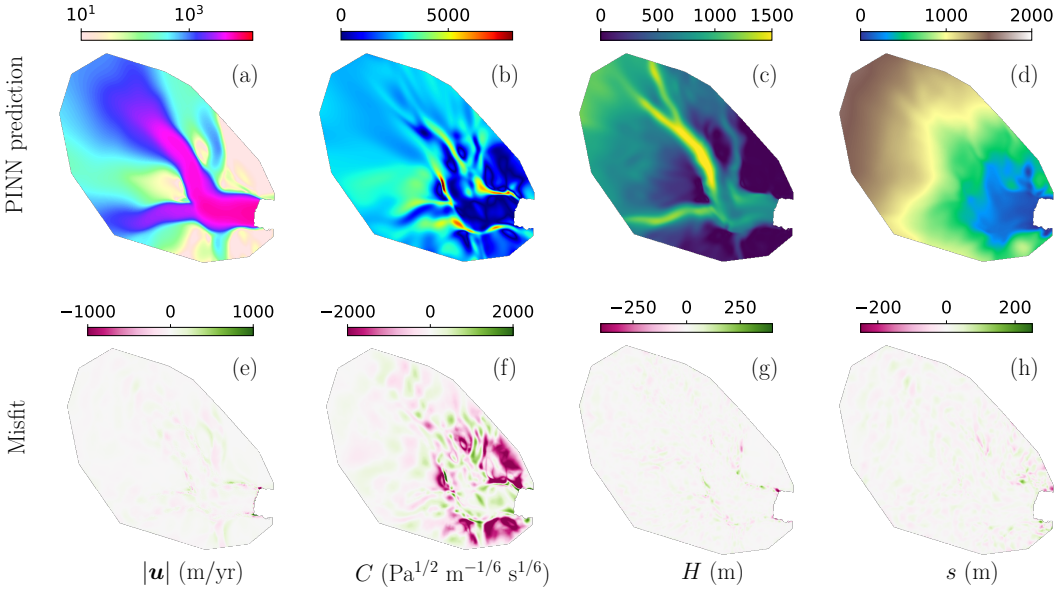

Figure 5. (a)-(d) Predictions of the PINN solving an inverse problem without exposure to the friction coefficient during training. (e)-(h) Corresponding misfits between the predictions and the "true" solution in Figure 2.

3.4 Inferring ice thickness

The flexibility of the PINN framework provides the possibility to infer the ice thickness H using ice velocity $\hat{\boldsymbol{u}}$, surface elevation $\hat{s}$, and friction coefficient $\hat{C}$. The PINN predictions and their corresponding misfits are shown in Figure 6. Similar to sections 3.2 and 3.3, the predictions of $\boldsymbol{u}$, s, and C align well with the training data, with relative errors of 3.5%, 4.3%, and 1.3%, respectively. The PINN's prediction of the ice thickness in Figure 6 (c) is a smoothed version of the true solution shown in Figure 2 (c). The misfit in Figure 6 (g) is distributed fairly evenly in the entire domain with an RMSE of 69.47 m, primarily located along the sharp transition of the H, such as the ice front and a part of the northern branch of Helheim Glacier.

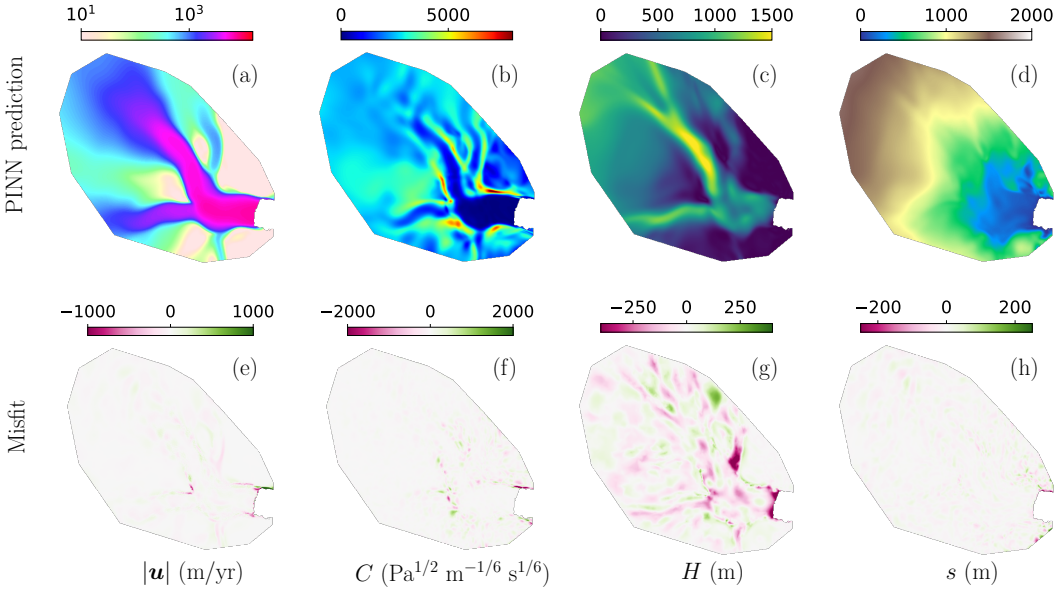

Figure 6. (a)-(d) Predictions of the PINN inferring ice thickness using ice velocity $\hat{\boldsymbol{u}}$, surface elevation $\hat{s}$, and friction coefficient $\hat{C}$ in the training procedure. (e)-(h) Corresponding misfits between the predictions and their corresponding reference data in Figure 2.

4 Discussion

4.1 A unified framework

The results presented above show how a single PINN architecture can solve both forward and inverse problems within the same framework. It is worth noting that there are no inherent distinctions between solving different types of problems within this framework. In other words, solving for ice velocity or inferring basal traction or ice thickness is implemented by switching on and off terms in the loss function during the training process. Depending on the training data provided, the PINN learns variables from both observational data and the underlying physics. This approach considerably simplifies the code development process compared to conventional numerical methods.

The training data serves as a foundational basis for the PINN to learn from, while the governing PDEs act as soft constraints, guiding the estimation of unknown param-

eters in the system. The PDE constraints provide additional relationships between all the variables involved, and act as a regularizing operator, particularly for the terms involving gradients (Karniadakis et al., 2021). For variables with available data during training, the PINN acts as a smooth interpolator. On the contrary, for variables without data, the PINN behaves as a solver, effectively satisfying the soft constraints imposed by the governing PDEs.

This unified framework, illustrated in Figure 1, offers flexibility for incorporating new variables and physics into the system. The addition of new variables involves introducing additional outputs from the neural network, while the inclusion of new physics requires adding an extra term to the loss function to assess the residual of the new governing equation. Furthermore, this framework can be readily extended to time-dependent problems by introducing time as an input variable to the neural network and evaluating time-dependent PDEs in the loss function.

4.2 Model performance

The results presented in section 3 show that the PINN is able to produce solutions for all three experiments with reasonable accuracy. The relative errors in all cases are below 5%. For the variables learned directly from the data (e.g., surface topography), the errors are evenly distributed throughout the entire domain, with some larger errors associated with steep changes in the data. On the other hand, when inferring solutions based on the PDE constraints, the errors depend on the location. In the forward run, the error in the predicted velocity ($\boldsymbol{u}$) is larger in the high-velocity region. Similarly, when inferring the ice thickness, larger errors are observed in the fast-flowing region and at sharp transition zones in the ice thickness.

However, in the basal friction inverse experiment, the errors in the inferred parameter C show a different pattern. Larger errors are observed in the slower-moving regions with thinner ice. This difference is likely due to the MSE of the velocity misfit that tends to prioritize the fast-flowing regions over the slower-moving ones. Considering the extensive range of ice velocities observed in Helheim Glacier, spanning five orders of magnitude, the solution for C in the inverse problem detailed in Figure 5 exhibits more substantial errors in regions characterized by low ice velocities (less than 10 m/yr) compared to those in the fast-moving regions. This situation is not unique to this approach, and traditional numerical methods also face this problem when inverting for the basal friction coefficient. The solution to tackle this problem in conventional inverse methods is to complement the $\mathcal{L}^2$ norm for the velocity misfit with a logarithmic norm of the velocity that will place more weight on the slow-moving regions (Morlighem et al., 2010). Additionally, the SSA equations ((1)) may not be a good approximation of the ice dynamics in slow-moving regions where vertical shear cannot be neglected. Since the flow velocity does not strongly depend on the friction coefficient in these slow-moving regions, the error is expected to be high.

The experiment in section 3.4 is particularly noteworthy as it demonstrates the capability of PINNs to infer ice thickness using momentum conservation (SSA). To our knowledge, this has not yet been achieved using conventional numerical methods. Together with the other experiments presented in section 3, these results underscore the inherent flexibility of the PINN framework. Ideally, this approach can be applied to infer any variable within the governing equation in a similar manner.

4.3 Dual inversion

In many real-world scenarios, the basal friction coefficient is unknown and needs to be inferred from surface observations, and the ice thickness is only known along flight lines, leaving large gaps that are generally filled using interpolation methods. Figure 7

illustrates all available flight tracks around Helheim Glacier, with dots representing resampled points at 200 m intervals along the tracks. These flight track data are notably sparse, even along the main branch of Helheim Glacier, where only one flight track is present in the center of the ice stream. Various numerical methods have been developed to leverage flight track data along with other observations to fill gaps in regions lacking direct measurements. Some examples include the BedMachine Greenland and Antarctica models (Morlighem et al., 2017, 2020), which use mass conservation principles to constrain ice thickness.

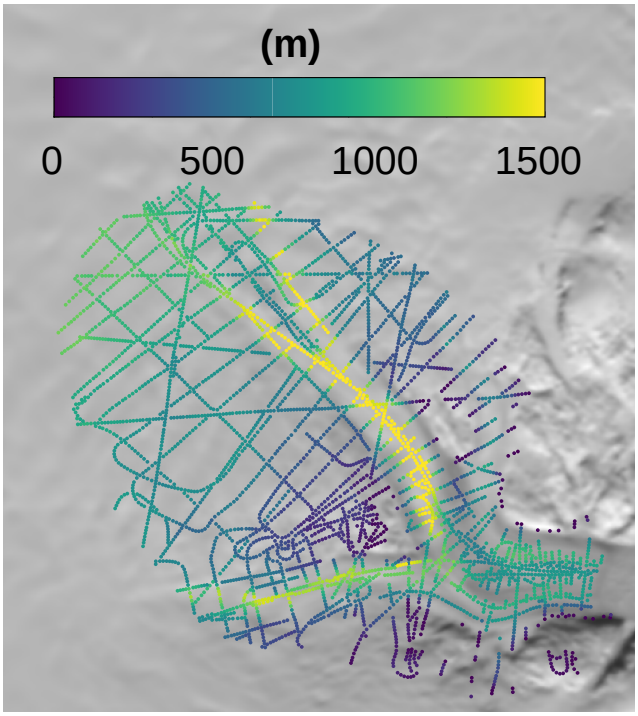

Figure 7. Available ice thickness data in the region of interest. The dots are resampled at 200 m intervals, overlaid with an image map from MEaSUREs MODIS Mosaic of Greenland (Haran et al., 2018).

Given the flexibility of the PINN, we perform one more test here to assess its ability to address a *dual* inversion problem. Here we would like to test the ability of the PINN to infer the basal friction coefficient, C, while simultaneously filling gaps in sparsely observed ice thickness, H. Following the same procedure as the ones described above, we expose the model to ice velocity, $\hat{\boldsymbol{u}}$, surface elevation, $\hat{s}$, and ice thickness only along flight tracks, $\bar{H}$, as shown in Figure 7. The predictions from the PINN and their corresponding misfits are presented in Figure 8. Notably, the PINN predictions for ice velocity and surface elevation align well with the true solutions (shown in Figure 2), and the RMSE of the misfits are 126.83 m/yr for the velocity and 22.08 m for the surface elevation. Both are below those obtained in the forward problem (193.75 m/yr and 26.99 m). The predicted ice thickness closely reproduces the shape and magnitude observed in the true solution as well. While the predicted friction coefficient shows a high misfit in slow-moving regions, as expected given the limitations of SSA in slow-moving regions discussed above, it aligns well with the true solution in fast-flow regions. The RMSE values for both C and H are comparable to those obtained in the individual inversions discussed in sections 3.3 and 3.4 (see Table 2).

It is important to note that only the ice velocity, surface elevation, and ice thickness along flight lines are incorporated into the training procedure and exposed to the PINN. The governing equation in the PINN is based on momentum conservation rather than mass conservation, which is the principle employed by BedMachine for inferring ice thickness. Consequently, discrepancies between the PINN predictions and the reference ice thickness from BedMachine are expected, constituting the likely primary reason for the observed misfit in Figure 8 (g). Furthermore, considering that the reference friction coefficient is inferred from ISSM using the ice thickness from BedMachine, differences are expected, particularly in regions where the two ice thickness datasets diverge.

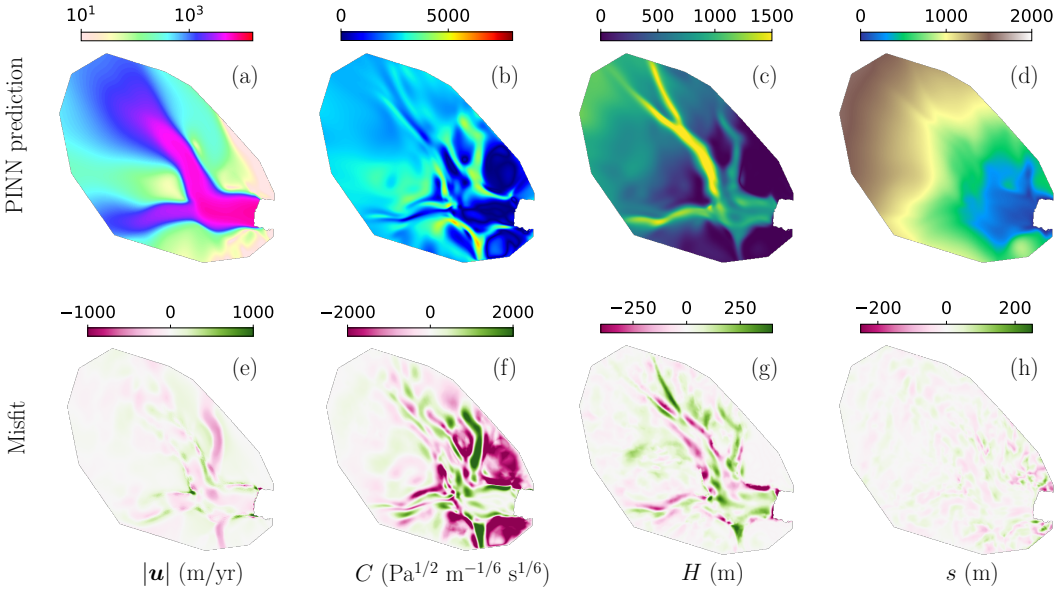

Figure 8. (a)-(d) Predictions of the PINN inferring ice thickness and basal friction coefficient using ice velocity $\hat{\boldsymbol{u}}$, surface elevation $\hat{s}$, and flight track data $\bar{H}$ (as in Figure 7) in the training procedure. (e)-(h) Corresponding misfits between the predictions and their corresponding reference data in Figure 2.

4.4 Limitations

While our study highlights the capabilities of PINNs in ice sheet modeling, certain limitations should be acknowledged. For the forward model, which is mathematically well-posed, traditional grid-based solvers clearly outperform PINNs (Karniadakis et al., 2021). For instance, while training the PINN for a forward problem (section 3.2) requires approximately 10 hours on one GPU, the same problem can be solved within minutes using established solvers like ISSM with 40 CPUs for a mesh of approximately $20,000$ elements. Another challenge is that the governing equations are imposed as soft constraints in the loss function and compete with the data misfit during the optimization, causing occasional non-convergence. Furthermore, it is well known that SSA serves as a reliable approximation for ice dynamics in fast-flowing regions but its assumptions break down in the interior of the ice sheet. Generalizing this approach to the entire Greenland Ice Sheet may necessitate the use of alternative physics or a combination of different physics to infer ice thickness, for example.

Future research directions will need to address the identified limitations and further enhance the application of PINNs in ice sheet modeling. To enhance its efficiency, the training process could be optimized and potentially integrate parallel computing strate-

gies for faster execution. The handling of PDEs as soft constraints in the PINN framework could be revised in order to mitigate convergence issues. Finally, improving the accuracy of the ice sheet interior will involve alternative physics or hybrid approaches that better capture the complexities of ice dynamics in slow-moving regions. These steps will collectively contribute to advancing the robustness, accuracy, and computational efficiency of PINNs for comprehensive ice sheet modeling.

5 Conclusion

This study explores several applications of PINNs in typical problems of ice sheet modeling. In contrast to traditional numerical methods, we utilize PINNs to construct a unified framework for both forward and inverse modeling. The inherent adaptability of PINNs is particularly easy to use and expand, enabling the inclusion of new physical parameters into the numerical model. This approach offers a promising avenue for enhancing the flexibility of ice sheet models and data assimilation, beyond the traditional categories of forward or inverse problems.

The dual inversion case presented in this study further demonstrates the ability of PINNs to simultaneously infer the basal friction coefficient and fill in gaps in partially sparse ice thickness observations. PINNs, with their capacity to integrate data misfit and physical principles, contribute to advancing numerical ice sheet modeling. This study suggests the potential of PINNs in improving our understanding of ice dynamics, contributing to more accurate predictions of future sea-level rise in glaciology and climate science.

6 Open Research

The data and the code of the simulations are available at `https://doi.org/10.5281/zenodo.10627691`. ISSM (Larour et al., 2009) is open source and available at `https://doi.org/10.5281/zenodo.7850841`.

Acknowledgments
This work was supported by the Heising Simons Foundation grant 2019-1161 and 2021-3059, and the National Science Foundation #2118285.

References

Åkesson, H., Morlighem, M., O'Regan, M., & Jakobsson, M. (2021). Future Projections of Petermann Glacier Under Ocean Warming Depend Strongly on Friction Law. *J. Geophys. Res. - Earth Surface*, *126*(6), e2020JF005921. Retrieved from `https://agupubs.onlinelibrary.wiley.com/doi/abs/10.1029/2020JF005921` doi: 10.1029/2020JF005921

Barnes, J. M., dos Santos, T. D., Goldberg, D., Gudmundsson, G. H., Morlighem, M., & De Rydt, J. (2021). The transferability of adjoint inversion products between different ice flow models. *Cryosphere*, *15*(4), 1975–2000. Retrieved from `https://tc.copernicus.org/articles/15/1975/2021/` doi: 10.5194/tc-15-1975-2021

Brondex, J., Gagliardini, O., Gillet-Chaulet, F., & Durand, G. (2017). Sensitivity of grounding line dynamics to the choice of the friction law. *J. Glaciol.*, *63*(241), 854-866. doi: 10.1017/jog.2017.51

Brondex, J., Gillet-Chaulet, F., & Gagliardini, O. (2019). Sensitivity of centennial mass loss projections of the Amundsen basin to the friction law. *Cryosphere*, *13*, 177-195. doi: 10.5194/tc-13-177-2019

Budd, W. F., Keage, P. L., & Blundy, N. A. (1979). Empirical studies of ice sliding.

J. Glaciol., *23*, 157-170.

Bueler, E., & Brown, J. (2009, JUL 31). Shallow shelf approximation as a "sliding law" in a thermomechanically coupled ice sheet model. *J. Geophys. Res.*, *114*, 1-21. doi: 10.1029/2008JF001179

Cheng, G., & Lotstedt, P. (2020, FEB 17). Parameter sensitivity analysis of dynamic ice sheet models - numerical computations. *CRYOSPHERE*, *14*(2), 673-691. doi: 10.5194/tc-14-673-2020

Colinge, J., & Blatter, H. (1998). Stress and velocity fields in glaciers: Part I. Finite-difference schemes for higher-order glacier models. *J. Glaciol.*, *44*(148), 448-456.

Cuffey, K. M., & Paterson, W. S. B. (2010). *The Physics of Glaciers, 4th Edition* (Butterworth-Heinemann, Ed.). Elsevier, Oxford.

Durand, G., Gagliardini, O., Zwinger, T., Le Meur, E., & Hindmarsh, R. C. A. (2009). Full Stokes modeling of marine ice sheets: influence of the grid size. *Ann. Glaciol.*, *50*(52), 109-114.

Eyring, V., Bony, S., Meehl, G. A., Senior, C. A., Stevens, B., Stouffer, R. J., & Taylor, K. E. (2016). Overview of the Coupled Model Intercomparison Project Phase 6 (CMIP6) experimental design and organization. *Geosci. Model Dev.*, *9*(5), 1937–1958. Retrieved from `http://www.geosci-model-dev.net/9/1937/2016/` doi: 10.5194/gmd-9-1937-2016

Frederikse, T., Landerer, F., Caron, L., Adhikari, S., Parkes, D., Humphrey, V. W., ... Wu, Y.-H. (2020, Aug 01). The causes of sea-level rise since 1900. *Nature*, *584*(7821), 393-397. Retrieved from `https://doi.org/10.1038/s41586-020-2591-3` doi: 10.1038/s41586-020-2591-3

Gagliardini, O., Cohen, D., Raback, P., & Zwinger, T. (2007, MAY 31). Finite-element modeling of subglacial cavities and related friction law. *J. Geophys. Res. - Earth Surface*, *112*(F2), 1-11. doi: 10.1029/2006JF000576

Glen, J. W. (1958). The flow law of ice: A discussion of the assumptions made in glacier theory, their experimental foundations and consequences. *IASH Publ*, *47*, 171–183.

Goldberg, D. N., & Sergienko, O. V. (2011). Data assimilation using a hybrid ice flow model. *Cryosphere*, *5*(2), 315-327. doi: 10.5194/tc-5-315-2011

Griewank, A., Juedes, D., & Utke, J. (1996). ADOL-C: A Package for the Automatic Differentiation of Algorithms Written in C/C++. *ACM Trans. Math. Software*, *22*(2), 131–167. Retrieved from `http://doi.acm.org/10.1145/229473.229474`

Haran, T., Bohlander, J., Scambos, T., Painter, T., & Fahnestock, M. (2018). *MEaSUREs MODIS Mosaic of Greenland (MOG) 2005, 2010, and 2015 Image Maps, Version 2.* Boulder, Colorado USA. NASA National Snow and Ice Data Center Distributed Active Archive Center. Retrieved from `https://doi.org/10.5067/9ZO79PHOTYE5` doi: 10.5067/9ZO79PHOTYE5

Howat, I. M., Negrete, A., & Smith, B. E. (2014). The Greenland Ice Mapping Project (GIMP) land classification and surface elevation datasets. *Cryosphere*, *8*(4), 1509-1518. Retrieved from `http://www.the-cryosphere.net/8/1509/2014/tc-8-1509-2014.html` doi: 10.5194/tc-8-1509-2014

Iwasaki, Y., & Lai, C.-Y. (2023, NOV 1). One-dimensional ice shelf hardness inversion: Clustering behavior and collocation resampling in physics-informed neural networks. *J. Comput. Phys.*, *492*. doi: 10.1016/j.jcp.2023.112435

Joughin, I., Smith, B. E., & Howat, I. M. (2018, February). A complete map of Greenland ice velocity derived from satellite data collected over 20 years. *J. Glaciol.*, *64*(243), 1-11. doi: 10.1017/jog.2017.73

Karniadakis, G. E., Kevrekidis, I. G., Lu, L., Perdikaris, P., Wang, S., & Yang, L. (2021, JUN). Physics-informed machine learning. *Nat. Rev. Phys.*, *3*(6), 422-440. doi: 10.1038/s42254-021-00314-5

Larour, E., Rignot, E., Seroussi, H., Morlighem, M., & Schiermeier, J. (2009). *ISSM*

website. (http://issm.jpl.nasa.gov)

Larour, E., Seroussi, H., Morlighem, M., & Rignot, E. (2012, Mar). Continental scale, high order, high spatial resolution, ice sheet modeling using the Ice Sheet System Model (ISSM). *J. Geophys. Res.*, *117*(F01022), 1-20. doi: 10.1029/2011JF002140

Lu, L., Meng, X., Mao, Z., & Karniadakis, G. E. (2021, MAR). DeepXDE: A Deep Learning library for solving differential equations. *SIAM Rev.*, *63*(1), 208-228. doi: 10.1137/19M1274067

MacAyeal. (1989, APR 10). Large-scale ice flow over a viscous basal sediment: Theory and application to Ice Stream B, Antarctica. *J. Geophys. Res.*, *94*(B4), 4071-4087.

MacAyeal, D. (2002, DEC). *Notes on ice stream inverse code finite element solution for ice stream equations.* (copy of a document printed in 2002)

Mangeney, A., & Califano, F. (1998, JAN 10). The shallow ice approximation for anisotropic ice: Formulation and limits. *J. Geophys. Res.*, *103*(B1), 691-705.

Morlighem, M., & Goldberg, D. (2023, June). Data Assimilation in Glaciology. In A. Ismail-Zadeh, F. Castelli, D. Jones, & S. Sanchez (Eds.), *Applications of data assimilation and inverse problems in the earth sciences.* Cambridge University Press.

Morlighem, M., Rignot, E., Binder, T., Blankenship, D., Drews, R., Eagles, G., ... Young, D. A. (2020). Deep glacial troughs and stabilizing ridges unveiled beneath the margins of the Antarctic ice sheet. *Nat. Geosci.*, *13*(2), 132–137. doi: 10.1038/s41561-019-0510-8

Morlighem, M., Rignot, E., Seroussi, H., Larour, E., Ben Dhia, H., & Aubry, D. (2010, JUL). Spatial patterns of basal drag inferred using control methods from a full-Stokes and simpler models for Pine Island Glacier, West Antarctica. *Geophys. Res. Lett.*, *37*(L14502), 1-6. doi: 10.1029/2010GL043853

Morlighem, M., Seroussi, H., Larour, E., & Rignot, E. (2013, SEP). Inversion of basal friction in Antarctica using exact and incomplete adjoints of a higher-order model. *J. Geophys. Res.*, *118*(3), 1746-1753. doi: 10.1002/jgrf.20125

Morlighem, M., Williams, C. N., Rignot, E., An, L., Arndt, J. E., Bamber, J. L., ... Zinglersen, K. B. (2017). BedMachine v3: Complete bed topography and ocean bathymetry mapping of Greenland from multi-beam echo sounding combined with mass conservation. *Geophys. Res. Lett.*, *44*(21), 11,051–11,061. Retrieved from `http://dx.doi.org/10.1002/2017GL074954` (2017GL074954) doi: 10.1002/2017GL074954

Mouginot, J., Rignot, E., Bjørk, A. A., van den Broeke, M., Millan, R., Morlighem, M., ... Wood, M. (2019). Forty-six years of greenland ice sheet mass balance from 1972 to 2018. *Proc. Natl. Acad. Sci.*. Retrieved from `https://www.pnas.org/content/early/2019/04/16/1904242116` doi: 10.1073/pnas.1904242116

Nowicki, S. M. J., Payne, A. J., Larour, E., Seroussi, H., Goelzer, H., Lipscomb, W. H., ... Shepherd, A. (2016, Dec). Ice Sheet Model Intercomparison Project (ISMIP6) contribution to CMIP6 . *Geosci. Model Dev.*, *9*, 4521-4545. doi: 10.5194/gmd-9-4521-2016

Petra, N., Zhu, H., Stadler, G., Hughes, T. J. R., & Ghattas, O. (2012). An inexact Gauss-Newton method for inversion of basal sliding and rheology parameters in a nonlinear Stokes ice sheet model. *J. Glaciol.*, *58*(211), 889-903. doi: 10.3189/2012JoG11J182

Raissi, M., Perdikaris, P., & Karniadakis, G. E. (2019, FEB 1). Physics-informed neural networks: A deep learning framework for solving forward and inverse problems involving nonlinear partial differential equations. *J. Comput. Phys.*, *378*, 686-707. doi: 10.1016/j.jcp.2018.10.045

Riel, B., Minchew, B., & Bischoff, T. (2021, NOV). Data-driven inference of the sechanics of slip slong glacier beds using physics-informed neural networks: case

study on Rutford Ice Stream, Antarctica. *J. Adv. Model. Earth Syst.*, *13*(11). doi: 10.1029/2021MS002621

Rignot, E., Mouginot, J., Scheuchl, B., van den Broeke, M., van Wessem, M. J., & Morlighem, M. (2019). Four decades of Antarctic Ice Sheet mass balance from 1979–2017. *Proc. Natl. Acad. Sci.*, *116*(4), 1095–1103. Retrieved from `https://www.pnas.org/content/early/2019/01/08/1812883116` doi: 10.1073/pnas.1812883116

Tarantola, A. (2005). *Inverse Problem Theory* (SIAM, Ed.). SIAM.

Vogel, C. R. (2002). *Computational Methods for Inverse Problems*. Philadelphia, PA, USA: Society for Industrial and Applied Mathematics.

Weertman, J. (1957, March). On the sliding of glaciers. *J. Glaciol.*, *3*, 33-38.

Yu, H., Rignot, E., Seroussi, H., & Morlighem, M. (2018). Retreat of Thwaites Glacier, West Antarctica, over the next 100 years using various ice flow models, ice shelf melt scenarios and basal friction laws. *Cryosphere*, *12*(12), 3861–3876. Retrieved from `https://www.the-cryosphere.net/12/3861/2018/` doi: 10.5194/tc-12-3861-2018

Neural Network

Update the weights

Optimization

Loss Function

$$\mathcal{L} = \mathcal{L}_{\mathbf{u}} + \mathcal{L}_g + \mathcal{L}_C + \mathcal{L}_\varphi$$

Data

Ice velocity

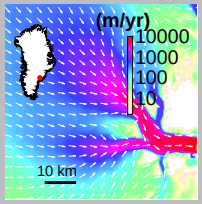

$$\mathcal{L}_{\boldsymbol{u}} = w_{\boldsymbol{u}}(\varepsilon_u + \varepsilon_v)$$

Surface elevation

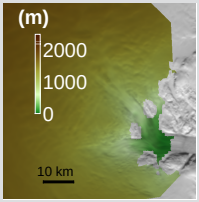

$$\mathcal{L}_g = w_g(\varepsilon_s + \varepsilon_H)$$

Friction coefficient

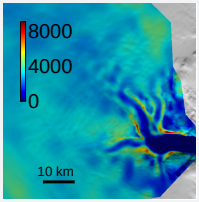

$$\mathcal{L}_C = w_C \varepsilon_C$$

Physics

$$\begin{cases} \nabla \cdot \boldsymbol{\sigma} + \boldsymbol{\tau}_b = \rho_i g H \nabla s, & \text{in } \Omega \\ \boldsymbol{n} \cdot \boldsymbol{\sigma} = (\bar{p}_i - \bar{p}_w)\boldsymbol{n} & \text{on } \Gamma \end{cases}$$

$$\mathcal{L}_\varphi = w_\Omega \varepsilon_\Omega + w_\Gamma \varepsilon_\Gamma$$

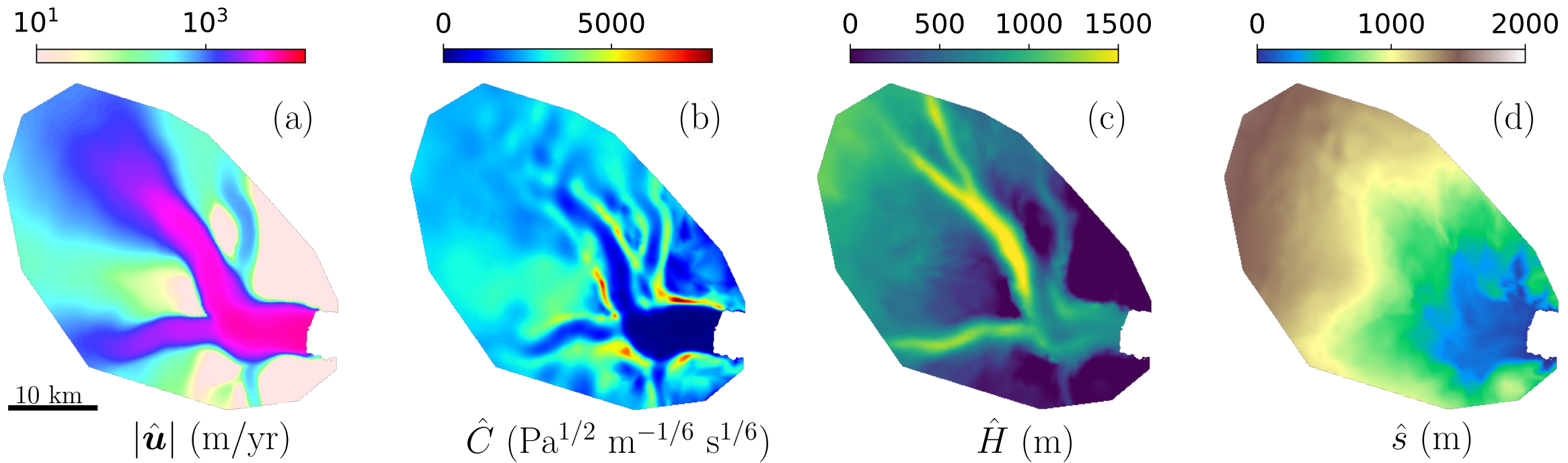
10^1
10^3
(a)
10 km
$|\hat{\boldsymbol{u}}|$ (m/yr)
0
5000
(b)
$\hat{C}$ (Pa$^{1/2}$ m$^{-1/6}$ s$^{1/6}$)
0
500
1000
1500
(c)
$\hat{H}$ (m)
0
1000
2000
(d)
$\hat{s}$ (m)

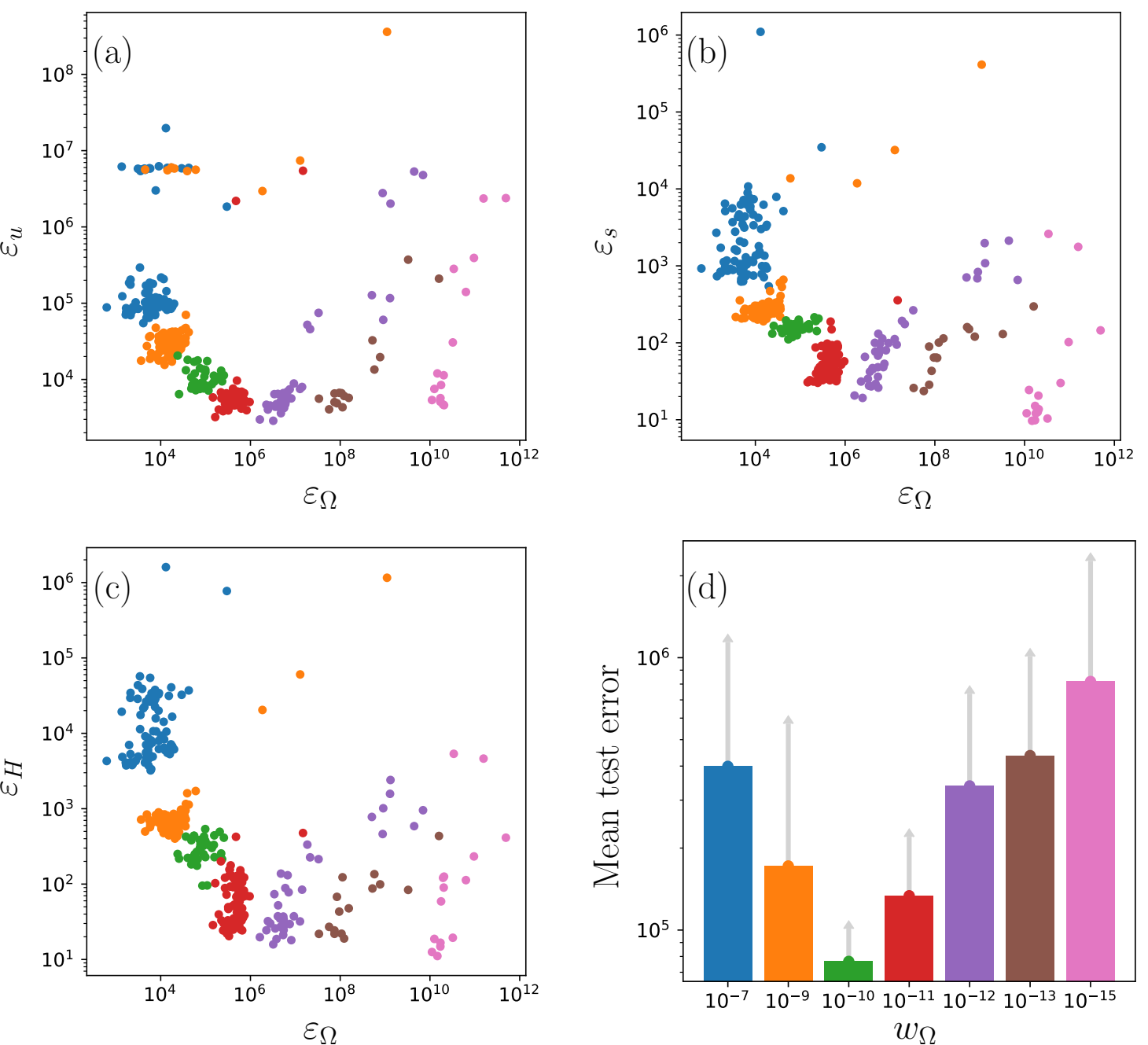
(a)
ε_u
ε_Ω
(b)
ε_s
ε_Ω
(c)
ε_H
ε_Ω
(d)
Mean test error
w_Ω
10^{-7} 10^{-9} 10^{-10} 10^{-11} 10^{-12} 10^{-13} 10^{-15}

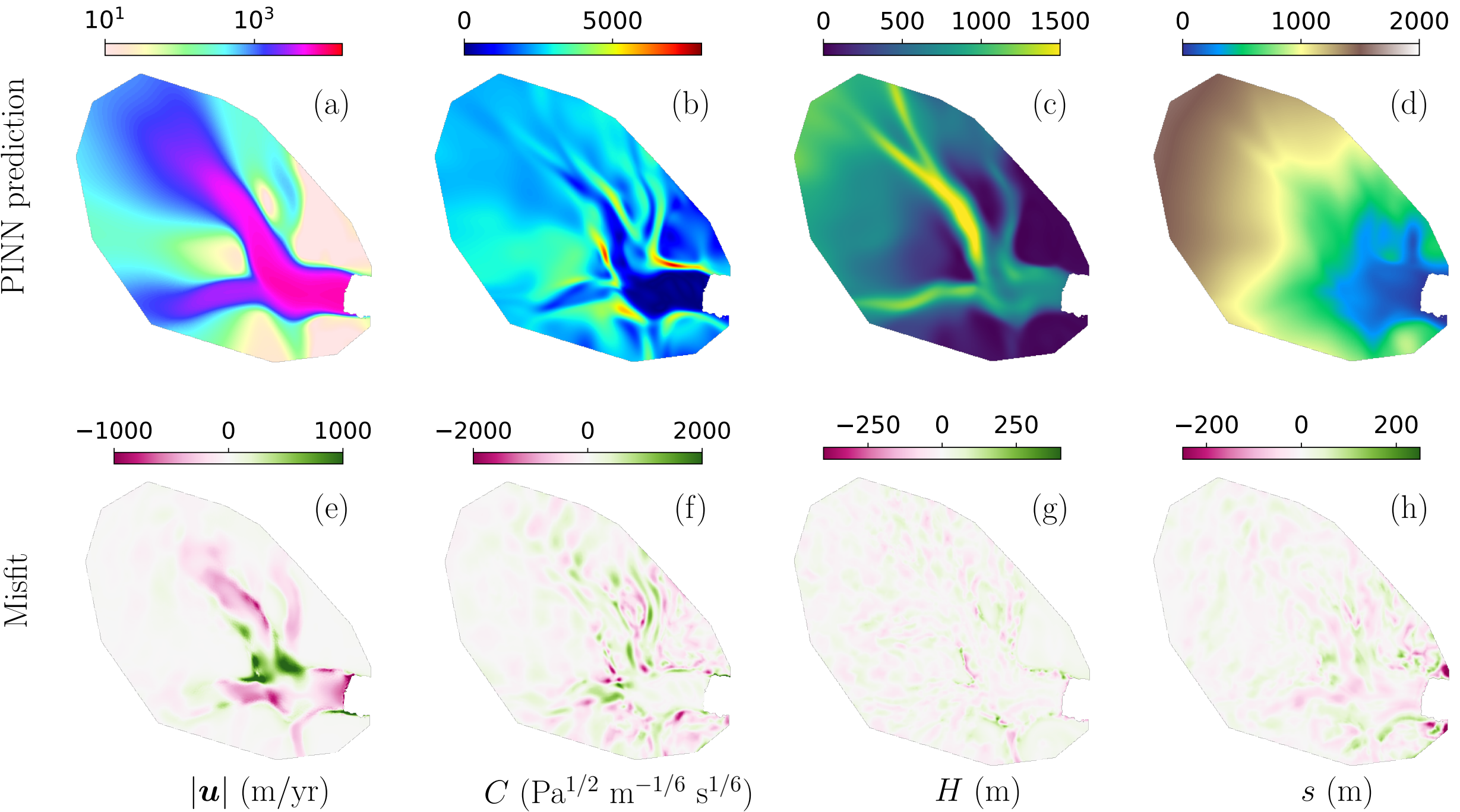
PINN prediction
Misfit
10^1
10^3
(a)
0
5000
(b)
0
500
1000
1500
(c)
0
1000
2000
(d)
−1000
0
1000
(e)
−2000
0
2000
(f)
−250
0
250
(g)
−200
0
200
(h)
$|\boldsymbol{u}|$ (m/yr)
C ($\mathrm{Pa}^{1/2}\ \mathrm{m}^{-1/6}\ \mathrm{s}^{1/6}$)
H (m)
s (m)

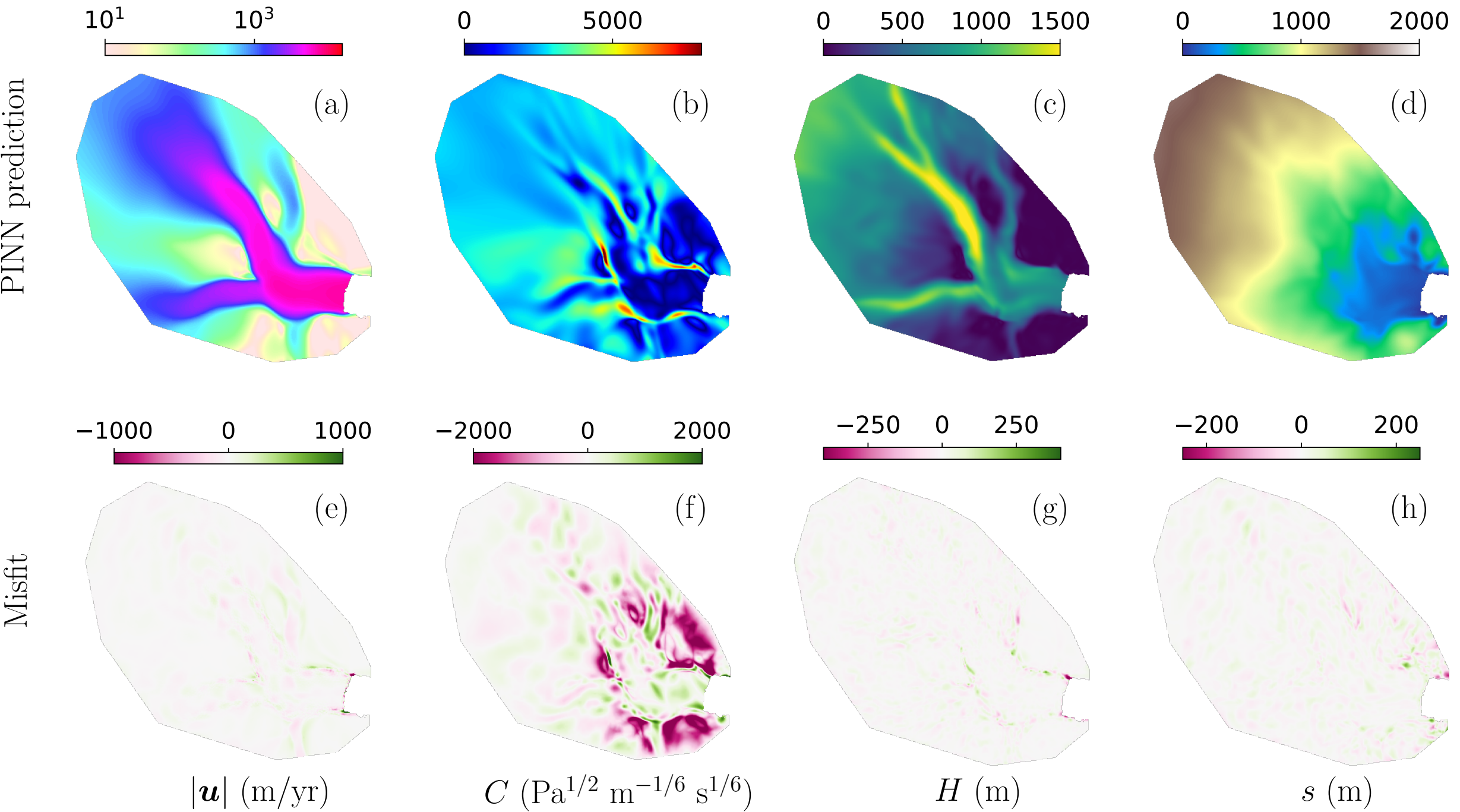
PINN prediction
Misfit
10^1
10^3
(a)
0
5000
(b)
0
500
1000
1500
(c)
0
1000
2000
(d)
−1000
0
1000
(e)
−2000
0
2000
(f)
−250
0
250
(g)
−200
0
200
(h)
$|\boldsymbol{u}|$ (m/yr)
C ($\mathrm{Pa}^{1/2}\ \mathrm{m}^{-1/6}\ \mathrm{s}^{1/6}$)
H (m)
s (m)

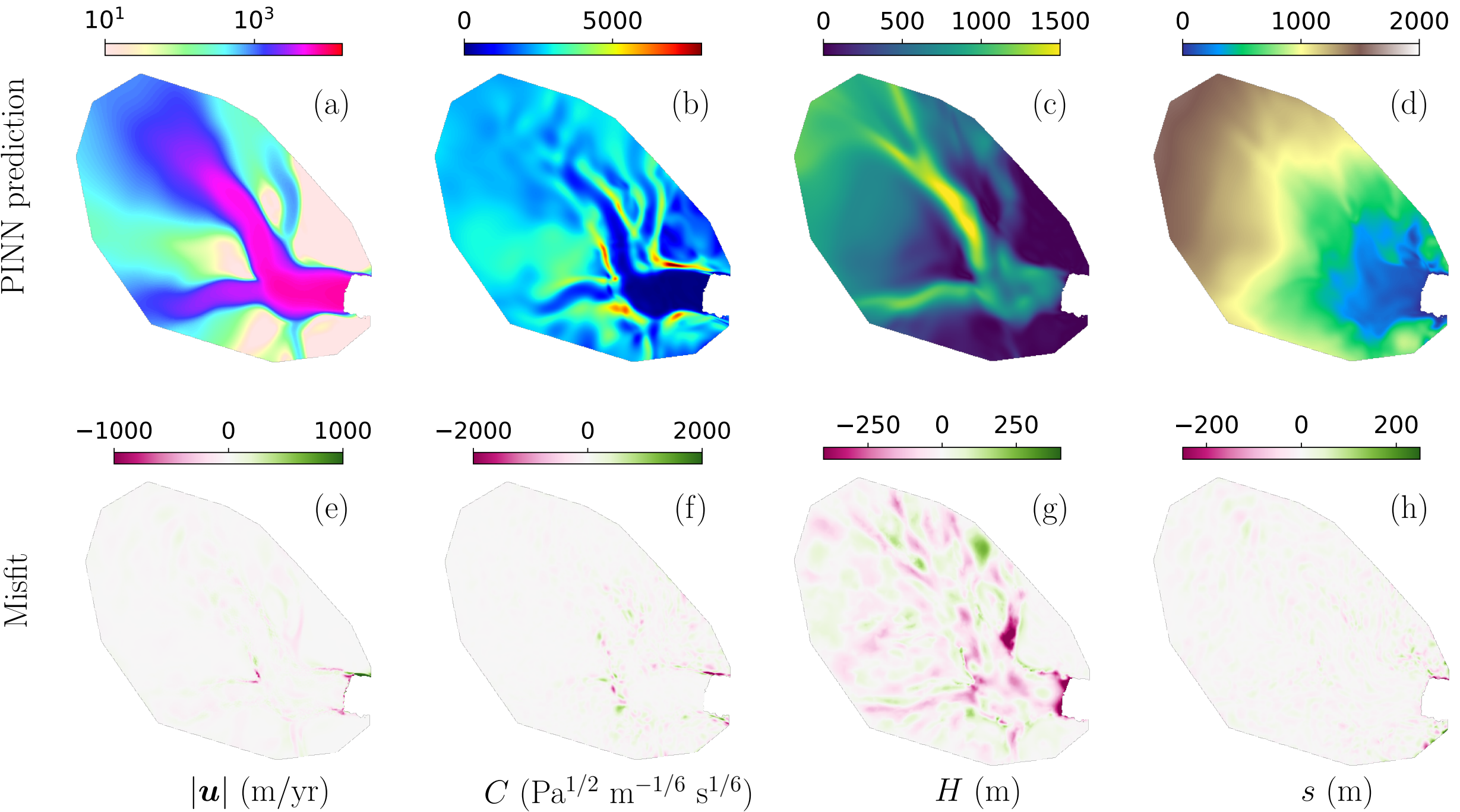
PINN prediction
Misfit
10^1
10^3
0
5000
0
500
1000
1500
0
1000
2000
(a)
(b)
(c)
(d)
−1000
0
1000
−2000
0
2000
−250
0
250
−200
0
200
(e)
(f)
(g)
(h)
$|\boldsymbol{u}|$ (m/yr)
C (Pa$^{1/2}$ m$^{-1/6}$ s$^{1/6}$)
H (m)
s (m)

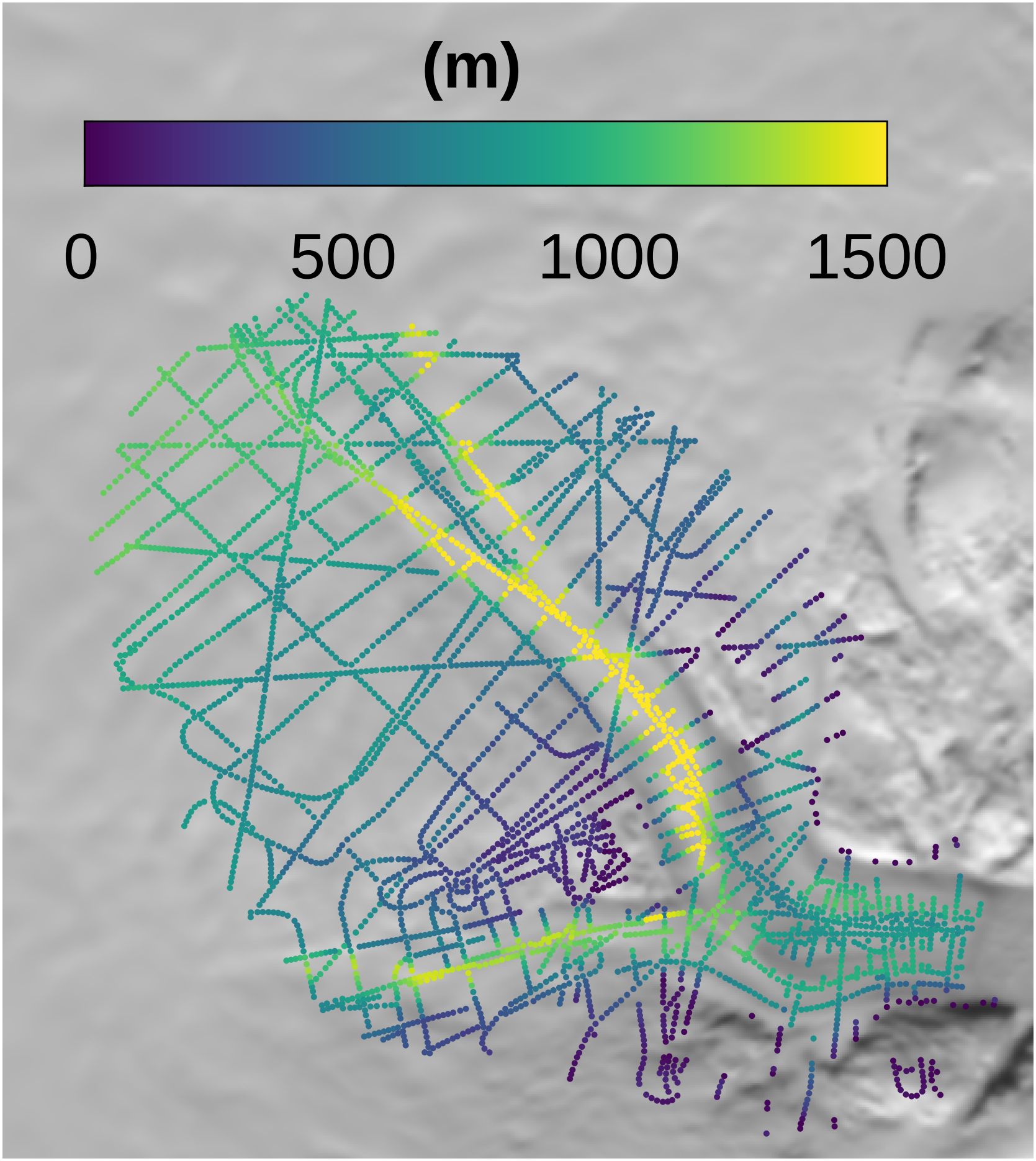
(m)
0
500
1000
1500

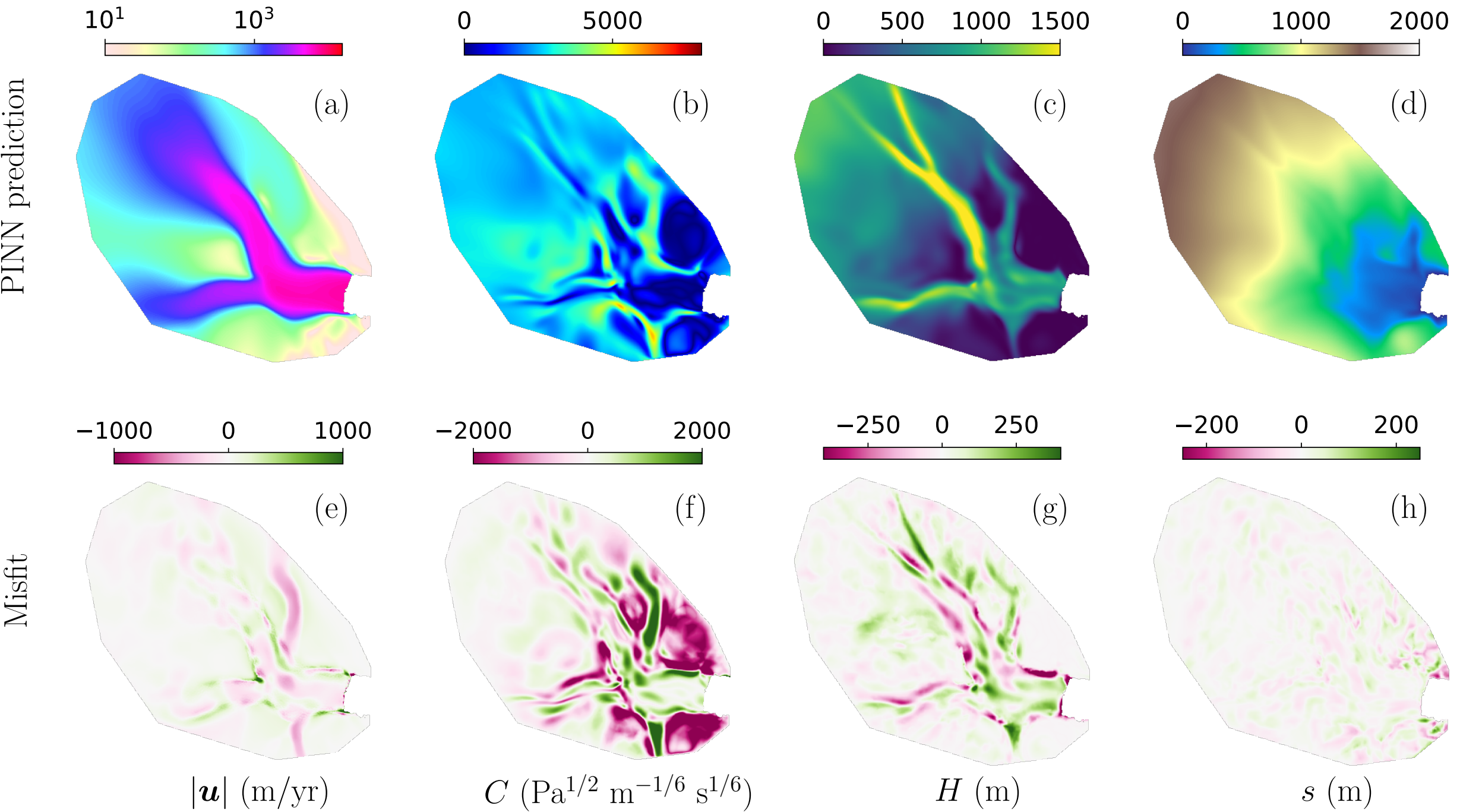
PINN prediction
Misfit
10^1
10^3
0
5000
0
500
1000
1500
0
1000
2000
(a)
(b)
(c)
(d)
−1000
0
1000
−2000
0
2000
−250
0
250
−200
0
200
(e)
(f)
(g)
(h)
$|\boldsymbol{u}|$ (m/yr)
C (Pa$^{1/2}$ m$^{-1/6}$ s$^{1/6}$)
H (m)
s (m)